Mon. Not. R. Astron. Soc. **365,** 647–652 (2006) doi:10.1111/j.1365-2966.2005.09750.x

Non-axisymmetric instabilities in shocked adiabatic accretion flows

Wei-Min Gu★ and Ju-Fu Lu

Department of Physics, Xiamen University, Xiamen 361005, China

Accepted 2005 October 12. Received 2005 October 12; in original form 2005 August 17

ABSTRACT

We investigate the linear stability of a shocked accretion flow on to a black hole in the adiabatic limit. Our linear analyses and numerical calculations show that, despite the post-shock deceleration, the shock is generally unstable to non-axisymmetric perturbations. The simulation results of Molteni, Tóth & Kuznetsov can be well explained by our linear eigenmodes. The mechanism of this instability is confirmed to be based on the cycle of acoustic waves between the corotation radius and the shock. We obtain an analytical formula to calculate the oscillation period from the physical parameters of the flow. We argue that the quasi-periodic oscillation should be a common phenomenon in accretion flows with angular momentum.

Key words: accretion, accretion discs – black hole physics – hydrodynamics – instabilities – shock waves.

1 INTRODUCTION

Hydrodynamic instabilities of shocked accretion flows may explain quasi-periodic oscillation (QPO) processes occurring in black hole candidates. The structure of stationary black hole accretion flows involving standing shocks was first described by Fukue (1987). Subsequently, shock studies have been made extensively in both inviscid and viscous accretion flows (Chakrabarti & Das 2004; Gu & Lu 2004, and references therein). However, even with the simple inviscid hypothesis, the stability of the shock is not fully understood. In the isothermal limit, Nakayama (1992) introduced a global instability between a sonic point and a shock, and found the criterion that 'post-shock acceleration causes instability', which was confirmed by the simulations of Nobuta & Hanawa (1994). Moreover, Nakayama (1994) investigated this instability in an adiabatic flow and claimed that such a criterion is also correct unless the shock is extremely strong. All the above works, however, were only for axisymmetric perturbations.

The pioneering work of Papaloizou & Pringle (1984) found a non-axisymmetric instability based on the acoustic cycle between the corotation radius and the boundary. The Papaloizou–Pringle instability (hereafter PPI) is known to take place in discs or tori, in which the radial velocity is initially zero. The mechanism of such an instability has been discussed extensively by Goldreich & Narayan (1985), Goldreich, Goodman & Narayan (1986), Narayan, Goldreich & Goodman (1987) and Kato (1987). The effect of radial advection on the PPI was investigated by Blaes (1987), who found that the PPI is strongly stabilized by advection at the inner boundary. Another type of non-axisymmetric instability was found in a spherical accretion flow by Foglizzo & Tagger (2000) and Foglizzo (2001, 2002), which is based on the cycle of entropy/vorticity perturbations and acoustic waves in the subsonic region between a stationary shock and a sonic surface. Recently, Gu & Foglizzo (2003, hereafter Paper I) studied a shocked accretion disc in the isothermal limit and found that the shock is generally linearly unstable to non-axisymmetric perturbations despite the post-shock deceleration. Paper I pointed out that such an instability is a form of PPI modified by advection and the presence of the shock. Apart from the above linear works, Molteni, Tóth & Kuznetsov (1999, hereafter MTK) performed two-dimensional simulations of a shocked adiabatic flow and found a non-axisymmetric instability. MTK simulations showed that the instability saturates at a low level, and a new asymmetric configuration develops, with a deformed shock rotating steadily. The mechanism of the instability, however, was not explained in MTK. They briefly mentioned a possible link with the non-axisymmetric disc instabilities studied by Blaes & Hawley (1988).

In this paper, we investigate the stability of a shocked accretion flow in the adiabatic and inviscid limit. We compare our linear results with the non-linear simulation results of MTK and manage to explain the different behaviours in their simulations. The paper is organized as follows. In Section 2, we present a set of linearized equations and boundary conditions. Subsequently, in Section 3, we present the linear results by numerically solving the equations. Finally, in Section 4, we summarize our conclusions and present a discussion.

2 EQUATIONS

An adiabatic flow around a black hole is considered in the pseudo-Newtonian potential introduced by Paczyński & Wiita (1980), $\Phi \equiv -GM/(r - r_{\rm g})$. Equations are made dimensionless by using the Schwarzschild radius and the speed of light as reference units, i.e. $r_{\rm g} \equiv 1$ and $c \equiv 1$. In this paper, the thickness of the flow is approximated as a constant for the sake of simplicity, as in Nakayama (1994), Blaes (1987), MTK and Paper I.

★E-mail: guwm@xmu.edu.cn

The stationary flow is described by the conservation of mass and the Bernoulli equation

$$\rho r \upsilon_{\rm r} = \text{const}, \tag{1}$$

$$e = \frac{\upsilon_{\rm r}^2}{2} + \frac{l^2}{2r^2} + \frac{c_{\rm s}^2}{\gamma - 1} - \frac{1}{2(r-1)} = \text{const}, \tag{2}$$

where ρ is the density, $\upsilon_{\rm r}$ is the radial velocity, $c_{\rm s} = (\gamma p/\rho)^{1/2}$ is the sound speed, l is the specific angular momentum and e is the Bernoulli constant. The structure of a stationary flow involving a standing shock can be obtained from the above equations by a given pair of (l, e) (see appendix A of MTK for details).

The continuity equation and the Euler equation are written as follows

$$\frac{\partial \rho}{\partial t} + \nabla \cdot (\rho \upsilon) = 0, \tag{3}$$

$$\frac{\partial \upsilon}{\partial t} + w \times \upsilon + \nabla \left[\frac{\upsilon^2}{2} + \frac{c_{\rm s}^2}{\gamma - 1} - \frac{1}{2(r-1)} \right] = c_{\rm s}^2 \nabla \frac{S}{\gamma}, \tag{4}$$

where w is the vorticity and S is the entropy.

Apart from vorticity perturbations and acoustic waves in an isothermal flow, entropy perturbations should appear in an adiabatic flow. Thus, the linearized equations here are slightly more complicated than those in Paper I. In order to write out the linearized equations in the simplest form, the two functions f, g are defined as follows

$$f \equiv \upsilon_{\rm r} \delta \upsilon_{\rm r} + \frac{2}{\gamma - 1} c_{\rm s} \delta c_{\rm s} + \upsilon_\varphi \delta \upsilon_\varphi, \tag{5}$$

$$g \equiv \frac{\delta \rho}{\rho} + \frac{\delta \upsilon_{\rm r}}{\upsilon_{\rm r}}, \tag{6}$$

where f is the perturbation of the Bernoulli constant and g is the perturbation of the mass accretion rate. The frequency ω' measured in the rotating frame is defined as

$$\omega' \equiv \omega - m\Omega, \tag{7}$$

where ω is the complex frequency of the perturbation, m is the azimuthal wavenumber and $\Omega \equiv l/r^2$ is the angular velocity. With the standard method of linear stability analysis, i.e. assuming perturbations to be proportional to $\mathrm{e}^{-{\rm i}\omega t + {\rm i}m\varphi}$, the following differential system is obtained:

$$\begin{aligned} \frac{\partial f}{\partial r} = & -\frac{{\rm i}\omega' \mathcal{M}^2}{\upsilon_{\rm r}(1-\mathcal{M}^2)} f + \frac{{\rm i}\omega \upsilon_{\rm r}}{1-\mathcal{M}^2} g \\ & + {\rm i}\omega \upsilon_{\rm r} \left(\frac{1}{1-\mathcal{M}^2} + \frac{1}{\gamma \mathcal{M}^2} \right) \delta S_{\rm sh} \exp\left(\int_{r_{\rm sh}}^{r} \frac{{\rm i}\omega'}{\upsilon_{\rm r}} {\rm d}r \right) \\ & + \frac{l}{r^2 \upsilon_{\rm r}(1-\mathcal{M}^2)} B_{\rm sh} \exp\left(\int_{r_{\rm sh}}^{r} \frac{{\rm i}\omega'}{\upsilon_{\rm r}} {\rm d}r \right), \end{aligned} \tag{8}$$

$$\begin{aligned} \frac{\partial g}{\partial r} = & \frac{\rm i}{\omega \upsilon_{\rm r}} \left[\frac{\omega'^2}{c_{\rm s}^2(1-\mathcal{M}^2)} - \frac{m^2}{r^2} \right] f - \frac{{\rm i}\omega' \mathcal{M}^2}{\upsilon_{\rm r}(1-\mathcal{M}^2)} g \\ & - \frac{{\rm i}\omega'}{\upsilon_{\rm r}(1-\mathcal{M}^2)} \delta S_{\rm sh} \exp\left(\int_{r_{\rm sh}}^{r} \frac{{\rm i}\omega'}{\upsilon_{\rm r}} {\rm d}r \right) \\ & - \frac{1}{\omega r^2 \upsilon_{\rm r}} \left[m + \frac{\omega' l}{c_{\rm s}^2(1-\mathcal{M}^2)} \right] B_{\rm sh} \exp\left(\int_{r_{\rm sh}}^{r} \frac{{\rm i}\omega'}{\upsilon_{\rm r}} {\rm d}r \right). \end{aligned} \tag{9}$$

Here, $B \equiv r \upsilon_{\rm r} w_z - {\rm i}\, m c_{\rm s}^2 \delta S/\gamma$, w_z is the vorticity along the rotation axis, $\mathcal{M} \equiv -\upsilon_{\rm r}/c_{\rm s}$ is the radial Mach number, and the subscript 'sh' denotes the shock position. The boundary conditions corresponding to a perturbed shock velocity $\Delta \upsilon_{\rm r}$ are obtained

$$f_{\rm sh} = (\upsilon_+ - \upsilon_-) \Delta \upsilon_{\rm r}, \tag{10}$$

$$g_{\rm sh} = \frac{\omega'}{\omega} \left(\frac{1}{\upsilon_+} - \frac{1}{\upsilon_-} \right) \Delta \upsilon_{\rm r}, \tag{11}$$

$$\delta S_{\rm sh} = -\frac{\gamma(\upsilon_+ - \upsilon_-)^2}{c_{\rm s+}^2 \upsilon_-} \left[\frac{\omega'}{\omega} + \frac{{\rm i}\upsilon_+}{\omega} \frac{{\rm d} \ln \mathcal{M}_+}{{\rm d}r} \right] \Delta \upsilon_{\rm r}, \tag{12}$$

$$B_{\rm sh} = 0, \tag{13}$$

where the subscripts '$-$' and '$+$' denote the pre-shock and post-shock values, respectively.

In addition to the two boundary conditions, equations (10) and (11), at the shock, a third equation is obtained from the critical condition at the sonic point

$$-\frac{\omega'}{\omega \upsilon_{\rm r}^2} f_{\rm son} + g_{\rm son} + \delta S_{\rm sh} \exp\left(\int_{r_{\rm sh}}^{r_{\rm son}} \frac{{\rm i}\omega'}{\upsilon_{\rm r}} {\rm d}r \right) = 0, \tag{14}$$

where the subscript 'son' denotes the sonic point. These three boundary conditions are used to numerically solve the differential system equations (8) and (9) and to determine the eigenfrequencies ω.

The methods for obtaining the above linearized equations and boundary conditions are similar to those in Paper I (see appendices B and C of Paper I for details).

3 NUMERICAL RESULTS

The standard Runge–Kutta method is used to integrate differential equations from the sonic point to the shock. In our calculations, the adiabatic index γ is fixed to be 4/3 as in MTK. Thus, the lowest post-shock Mach number (corresponding to extremely strong shocks) is $\mathcal{M}_{\rm sh} = [(\gamma - 1)/2\gamma]^{1/2} = 0.354$. Table 1 presents a sample of 15 shocked accretion flows, of which cases 1–11 were exactly taken from table 1 of MTK. As shown in Table 1, for cases 1–11, the ranges of the post-shock Mach number $\mathcal{M}_{\rm sh}(0.493, 0.760)$ and the minimum Mach number in the subsonic region between the sonic point and the shock $\mathcal{M}_{\rm min}(0.255, 0.650)$ are slightly narrow compared with the theoretical ranges, $\mathcal{M}_{\rm sh}(0.354, 1)$ and $\mathcal{M}_{\rm min}(0, 1)$, respectively. Thus, cases 12–15 are added to Table 1 to make the ranges wider, i.e. $\mathcal{M}_{\rm sh}(0.372, 0.923)$ and $\mathcal{M}_{\rm min}(0.034, 0.650)$. Our linear results for $m = 1$ and MTK simulation results are listed in columns 6 and 7 of Table 1, respectively.

Fig. 1 shows the domain (l, e) of the angular momentum and the Bernoulli constant for which an adiabatic flow, subsonic far from the accretor, may be accreted on to a black hole through a stationary shock. Each point between the two solid lines represents an inner shock (post-shock acceleration) and an outer shock (post-shock deceleration). Because the inner shock was already found to be unstable to axisymmetric perturbations, we concentrate on the stability of the outer shock against non-axisymmetric perturbations.

3.1 Linear results compared with MTK simulation results

As shown in Table 1, our linear numerical calculations find that cases 1–14 are unstable and case 15 is stable, whereas the non-linear simulations of MTK found that cases 1–11 are unstable except for case 9. The agreement of linear and non-linear results can be understood as follows. In their simulations, $\mathcal{M}_{\rm sh}$ of the stable flow (case 9) is the largest (among cases 1–11). Similarly, in our linear calculations,

Table 1. A sample of 15 shocked accretion flows for numerical calculations.

Case	$r_{\rm sh}$	l	$\mathcal{M}_{\rm sh}$	$\mathcal{M}_{\rm min}$	$m = 1$ linear results	MTK simulation results
1	5.3	1.7770	0.651	0.650	Unstable	Regular oscillation
2	5.3	1.8000	0.574	0.572	Unstable	Regular oscillation
3	5.3	1.8100	0.539	0.536	Unstable	Beating
4	5.3	1.8225	0.493	0.489	Unstable	Irregular
5	7.8	1.8000	0.629	0.556	Unstable	Regular oscillation
6	7.8	1.8100	0.595	0.520	Unstable	Beating
7	7.8	1.8200	0.560	0.482	Unstable	Beating
8	12.7	1.8200	0.684	0.465	Unstable	Regular oscillation
9	17.2	1.8255	0.760	0.439	Unstable	Nearly stable
10	23.4	1.8620	0.710	0.294	Unstable	Regular oscillation
11	23.4	1.8720	0.664	0.255	Unstable	Leaves domain
12	19.9	1.9200	0.372	0.074	Unstable	–
13	34.8	1.9400	0.405	0.034	Unstable	–
14	16.8	1.8900	0.481	0.183	Unstable	–
15	19.8	1.8000	0.923	0.535	Stable	–

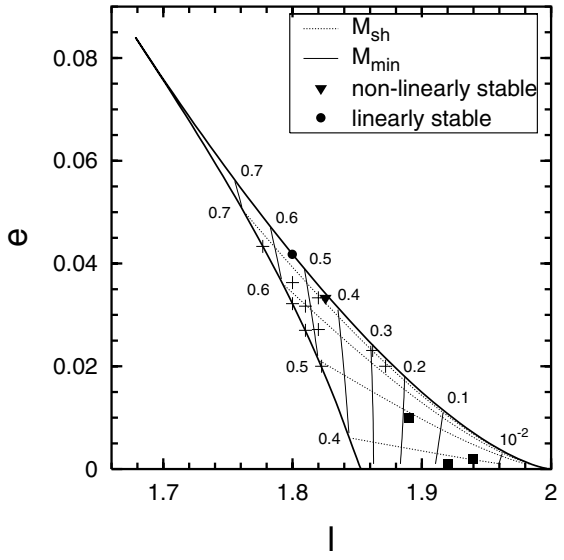

Figure 1. The two thick solid lines are the threshold for shock-included solutions. The dotted lines measure the shock strength by the value of $\mathcal{M}_{\rm sh}$ indicated on the left. The thin solid lines correspond to the value of the minimum Mach number $\mathcal{M}_{\rm min}$ indicated on the right. The 10 crosses represent cases 1–8 and 10–11, which are unstable in MTK simulations. The filled triangle represents case 9, which is stable in MTK simulations. The three filled squares represent cases 12–14, which together with cases 1–11 are linearly unstable. The filled circle represents case 15, which is linearly stable.

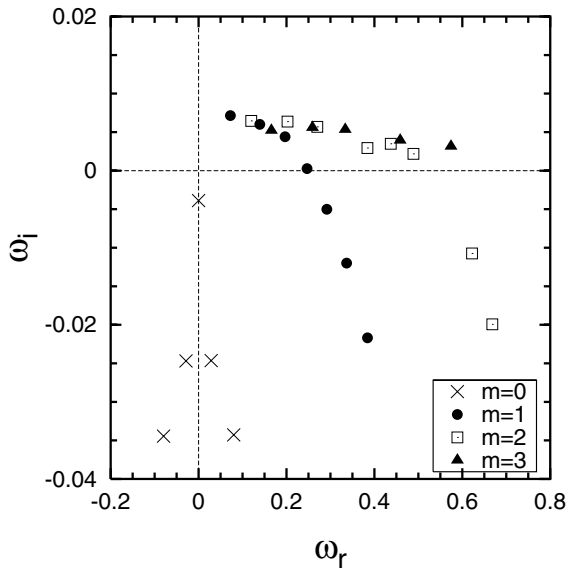

Figure 2. Case 5: eigenspectrum for $0 \leqslant m \leqslant 3$.

$\mathcal{M}_{\rm sh}$ of the stable flow (case 15) is also the largest (among cases 1–15). Thus, both linear and non-linear results indicate that the shock is generally unstable to non-axisymmetric perturbations except for $\mathcal{M}_{\rm sh} \to 1$, i.e. very weak shock. We therefore argue that there is no essential difference between the linear and non-linear results. This general instability is even clear from Fig. 1, which shows that both the linearly stable shock (case 15, filled circle) and the non-linearly stable shock (case 9, filled triangle) locate very close to the right border, whereas the other unstable shocks stand everywhere except for a very narrow region close to the right $\mathcal{M}_{\rm sh} \sim 1$ border.

As a typical example, the eigenspectrum of case 5 is shown in Fig. 2 for perturbations $0 \leqslant m \leqslant 3$. The shock is linearly stable to axisymmetric perturbations ($m = 0$), which coincides with the criterion 'post-shock acceleration causes instability'. Despite the post-shock deceleration, however, the shock is found to be unstable to non-axisymmetric perturbations with $m = 1$, 2, 3. The MTK simulations found that, for case 5, the perturbed axisymmetric shock will finally change into an $m = 1$ deformed shock. Such a non-linear evolution can be well explained by our numerically obtained eigenmodes. As shown in Fig. 2, the fastest growth rate corresponds to $m = 1$, $\omega = 0.0725 + 0.00715$ i, which indicates that the $m = 1$ perturbations should dominate over the others.

To understand the different behaviours of perturbed shocks in MTK simulations, we focus on cases 1–7 because there exists continuous change from 1 to 4 and from 5 to 7, respectively. Fig. 3 shows that the fastest growth rate corresponds to $m = 1$ for cases 1 and 5. For the other five cases, however, the fastest growth rate does not correspond to $m = 1$. In other words, among cases 1–7, $m = 1$ perturbations dominate for cases 1 and 5. As shown in Table 1, MTK simulations found that the perturbed shock will change into an $m = 1$ deformed shock for cases 1, 2 and 5. Comparing the linear results with simulations, we therefore conclude that the non-linear

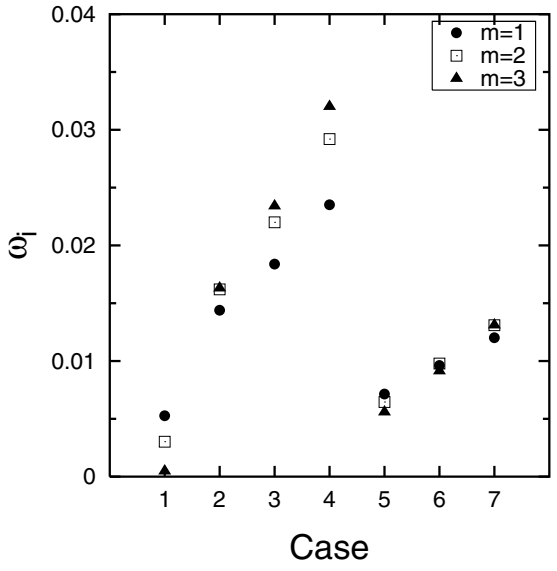

Figure 3. Cases 1–7: growth rates for $1 \leqslant m \leqslant 3$.

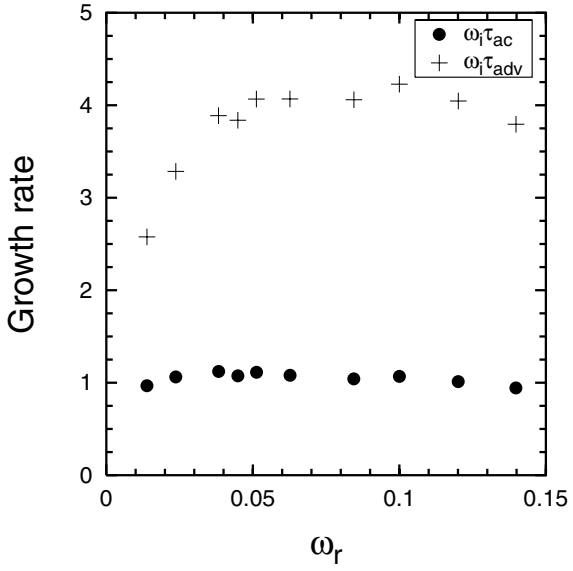

Figure 4. Case 12: growth rates compared to $\tau_{\rm ac}$ and $\tau_{\rm adv}$.

behaviours are determined by the fastest growth rate. The $m = 1$ deformed shock, i.e. 'regular oscillation', should come into being when the fastest growth rate corresponds to $m = 1$. On the contrary, other types such as 'beating' should appear when the fastest growth rate does not correspond to $m = 1$.

The only inconsistent solution is case 2. As shown in Table 1 and Fig. 3, from case 1 to 4, the transition direction of the instability is identical for the linear and non-linear results, i.e. from $m = 1$ dominance to $m \neq 1$ dominance. The transition point locates between cases 1 and 2 in our linear calculations, but between cases 2 and 3 in MTK simulations. As mentioned in MTK, the average distance of the final deformed shock will be slightly larger than before. Thus, the outmoving of the shock may account for the above quantitative difference.

3.2 Instability mechanism

In the isothermal work of Paper I, the mechanism of the instability was already found to be based on the cycle of acoustic waves between the corotation radius and the shock. Such a mechanism can be confirmed by the new evidence of Fig. 4, which shows 10 unstable eigenmodes for $m = 1$ of case 12. We choose case 12 because the shock is far away from the sonic point and $\mathcal{M}_{\rm min}$ is low enough, and thus the flow has a number of unstable eigenmodes. Different from the rough time-scales $\tau_{\rm ac}$ and $\tau_{\rm adv}$ in Paper I, here we numerically calculate the exact values of the time of the purely acoustic cycle $\tau_{\rm ac}$ and the advective-acoustic cycle $\tau_{\rm adv}$:

$$\tau_{\rm ac} = \int_{r_{\rm co}}^{r_{\rm sh}} \left(\frac{1}{c_{\rm s} + |\upsilon_{\rm r}|} + \frac{1}{c_{\rm s} - |\upsilon_{\rm r}|} \right) {\rm d}r, \tag{15}$$

$$\tau_{\rm adv} = \int_{r_{\rm co}}^{r_{\rm sh}} \left(\frac{1}{|\upsilon_{\rm r}|} + \frac{1}{c_{\rm s} - |\upsilon_{\rm r}|} \right) {\rm d}r. \tag{16}$$

Here the corotation radius $r_{\rm co}$ of the perturbation is defined by $\omega = m\,\Omega_0$, with $\Omega_0 \equiv \Omega(r_{\rm co})$:

$$r_{\rm co} \equiv \left(\frac{lm}{\omega_{\rm r}} \right)^{1/2}. \tag{17}$$

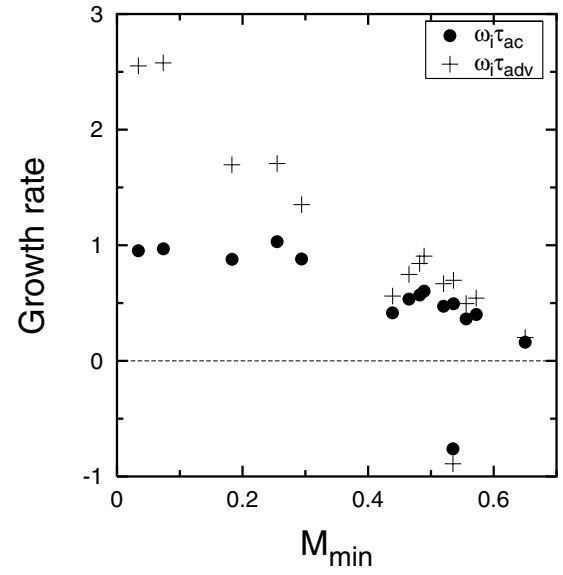

Figure 5. Cases 1–15: growth rates of the most unstable mode compared to $\tau_{\rm ac}$ and $\tau_{\rm adv}$.

Fig. 4 shows that the growth time is always around $\tau_{\rm ac}$, i.e. $\omega_i\,\tau_{\rm ac} \approx 1$, but can be much shorter than $\tau_{\rm adv}$, i.e. $\omega_i\,\tau_{\rm adv} \gtrsim 1$, which strongly indicates that the mechanism is based on the purely acoustic cycle, not the advective-acoustic cycle. However, such evidence was not noticed in Paper I.

To have a global view, for $m = 1$, the most unstable modes of all the 15 flows are included in Fig. 5, which shows that for low $\mathcal{M}_{\rm min}$, i.e. $\tau_{\rm ac} \ll \tau_{\rm adv}$, the most unstable mode well matches $\omega_i\,\tau_{\rm ac} \approx 1$. This result again confirms the above-mentioned mechanism in adiabatic flows. The value of $\omega_i\,\tau_{\rm ac}$, however, evidently decreases as $\mathcal{M}_{\rm min} \to 1$, which implies that the instability is suppressed by advection. Different from fig. 5 of Paper I, in Fig. 5 here we choose $\mathcal{M}_{\rm min}$ as abscissa instead of $\mathcal{M}_{\rm sh}$ because an adiabatic flow with $\gamma = 4/3$ cannot have very low $\mathcal{M}_{\rm sh}$ and, more importantly, $\mathcal{M}_{\rm min}$ implies the strength of advection.

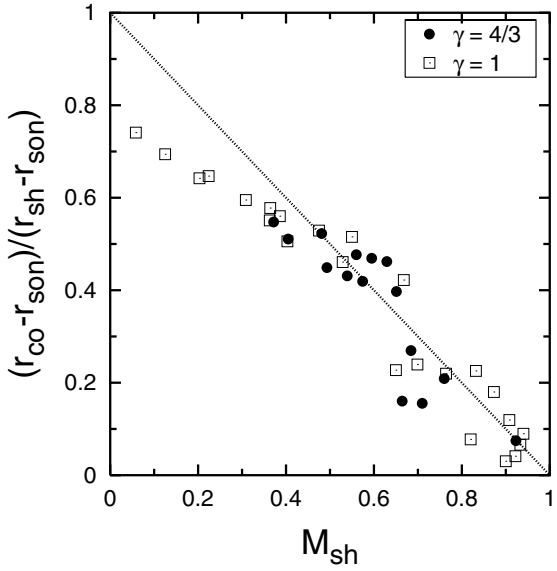

Figure 6. The positions of the corotation radius of the most unstable mode are indicated for 15 adiabatic flows (circles) and 24 isothermal flows (squares). The dotted line corresponds to $(r_{\rm co}-r_{\rm son})/(r_{\rm sh}-r_{\rm son})=1-\mathcal{M}_{\rm sh}$.

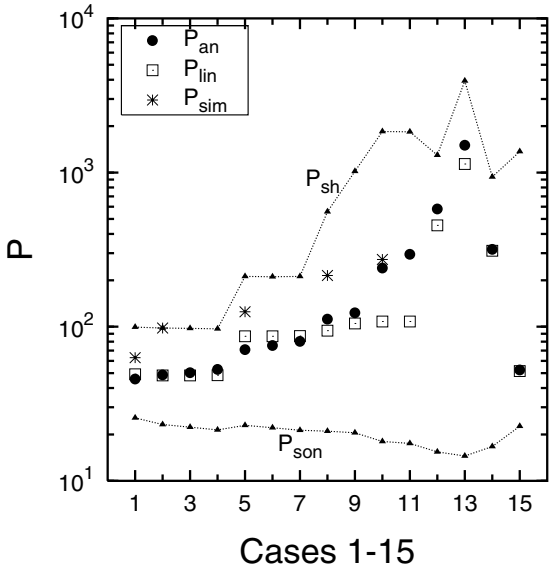

Figure 7. Three types of periods for cases 1–15: the analytical $P_{\rm an}$, the linear $P_{\rm lin}$ and the MTK simulation results $P_{\rm sim}$. The upper and lower dotted lines correspond to $P_{\rm sh}$ and $P_{\rm son}$, respectively.

3.3 Oscillation period

The growth rate is relevant to the imaginary part of the eigenfrequency ω_i, whereas the oscillation period is relevant to the real part $\omega_{\rm r}$ (or $r_{\rm co}$). Fig. 6 includes all the 15 flows in Table 1 together with the 24 isothermal flows from Paper I, which shows the relationship between $r_{\rm co}$, $r_{\rm son}$, $r_{\rm sh}$ and $\mathcal{M}_{\rm sh}$. For $\mathcal{M}_{\rm sh}$ which is not very low, Fig. 6 suggests the following good approximation:

$$\frac{r_{\rm co}-r_{\rm son}}{r_{\rm sh}-r_{\rm son}}=1-\mathcal{M}_{\rm sh}. \tag{18}$$

Thus, an analytical formula for calculating the oscillation period is obtained:

$$P_{\rm an}=\frac{2\pi r_{\rm co}^2}{l}=\frac{2\pi}{l}\left[r_{\rm sh}-(r_{\rm sh}-r_{\rm son})\mathcal{M}_{\rm sh}\right]^2. \tag{19}$$

The lowest post-shock Mach number $\mathcal{M}_{\rm sh}=[(\gamma-1)/2\gamma]^{1/2}$ implies that only an isothermal flow or a flow with $\gamma\rightarrow 1$ can have an extremely low value of $\mathcal{M}_{\rm sh}$. Thus, equation (19) should work well in normal adiabatic flows with $4/3\leqslant\gamma\leqslant 5/3$. In addition, we define the linear period $P_{\rm lin}$ for $m=1$ as follows:

$$P_{\rm lin}\equiv\frac{2\pi}{\omega_{\rm r}^{\rm max}}, \tag{20}$$

where $\omega_{\rm r}^{\rm max}$ is the real part of the eigenfrequency corresponding to the most unstable mode.

The different types of periods are shown in Fig. 7. The lower and upper dotted lines correspond to the rotation period at the sonic point $P_{\rm son}=2\pi r_{\rm son}^2/l$ and at the shock $P_{\rm sh}=2\pi r_{\rm sh}^2/l$, respectively. This figure shows that both the linear $P_{\rm lin}$ and the non-linear $P_{\rm sim}$ always locate between $P_{\rm son}$ and $P_{\rm sh}$ (except for case 2), which is in good agreement with the condition that the corotation radius should locate between the sonic point and the shock. Fig. 7 demonstrates that the analytical period $P_{\rm an}$ is a good approximation for the linear period $P_{\rm lin}$ and not far from the non-linear period $P_{\rm sim}$. As mentioned in MTK, the average distance of the final deformed shock will be slightly larger than before. For example, in case 5, the final distance $r_{\rm sh}$ varies between 9 and 11, which is larger than the original value of 7.8. If this outmoving is taken into consideration, $P_{\rm sh}=2\pi r_{\rm sh}^2/l$ should therefore be even larger; thus, $P_{\rm sim}$ of case 2 should indeed locate between $P_{\rm son}$ and $P_{\rm sh}$. Furthermore, the outmoving well explains why $P_{\rm sim}$ is always larger than $P_{\rm lin}$ and $P_{\rm an}$ (as shown in Fig. 7).

4 CONCLUSIONS AND DISCUSSION

The main results can be summarized as follows.

(i) The general non-axisymmetric instability of the outer shock, which was previously found by non-linear simulations for adiabatic flows and linear calculations for isothermal flows, is confirmed in the present paper by linear calculations for adiabatic flows.

(ii) The simulation results of MTK are well explained by our numerically obtained linear eigenmodes.

(iii) New evidence is shown to support the argument in Paper I for the mechanism that the instability is based on the cycle of acoustic waves between the corotation radius and the shock.

(iv) An analytical formula is obtained to calculate the oscillation period P from the physical parameters $r_{\rm son}$, $r_{\rm sh}$, l and $\mathcal{M}_{\rm sh}$.

The present work is for an inviscid accretion flow with a standing radial shock. Realistic astrophysical accretion flows must have viscosity, and it remains controversial whether a standing shock can indeed form in a viscous accretion flow around a black hole. In an accretion flow, the gravitational potential energy is converted to kinetic and thermal energy of the accreting gas. Based on the energy consideration, Narayan, Mahadevan & Quataert (1998) identified three regimes of accretion: the radiative cooling-dominated accretion flow, the advection-dominated accretion flow (ADAF) and the low energy generated accretion flow. For cooling-dominated flows or ADAFs, the released gravitational potential energy is mainly converted to thermal energy by viscous stresses and then radiated away or advected into the central black hole. Except for the region very close to the black hole ($\lesssim 5\,r_{\rm g}$), the radial motion of these two types of accretion flow remains subsonic because of the low kinetic energy. This is the physical reason why there are no shocks in the ADAF-thin disc solutions (e.g. Narayan, Kato & Honma 1997, hereafter NKH),

and this result does not rely on the mathematical technology. In fact, Lu, Gu & Yuan (1999) recovered the shock-free ADAF-thin disc solutions using the Runge–Kutta method (by adjusting the specific angular momentum j accreted by the black hole and the sonic point $r_{\rm son}$ of an ADAF to match a thin disc at the outer boundary), which are identical with those in NKH using the relaxation method (by assuming the value of the outer boundary $r_{\rm out}$ and the conditions at $r_{\rm out}$, and then solving the set of equations and calculating out j and $r_{\rm son}$ as eigenvalues). In our opinion, a standing shock may form if the original flow belongs to the third regime mentioned above, i.e. a low energy generated accretion flow. If the flow has very low angular momentum l at large distance, i.e. close to Bondi accretion (in an ADAF l is not very low; see fig. 2 of NKH), the gravitational force dominates over the centrifugal force. The flow is accelerated efficiently in the radial direction and becomes supersonic far from the central black hole (Yuan 1999); then a shock is likely to develop. Such a flow is a low energy generated one because the released gravitational potential energy is mainly converted to kinetic energy rather than thermal energy. NKH have also agreed that this is the situation in which a shock can indeed be physical. Thus, we believe that flows with low angular momentum and weak viscosity (i.e. low energy generation) will have shocks.

It is well known that the PPI occurs with either an inner or an outer reflecting boundary, or even more efficiently with both. The boundary in the present paper is a standing shock. However, a shock is not the only type of boundary which can reflect acoustic waves. For example, the transition from a Shakura–Sunyaev disc (Shakura & Sunyaev 1973) to an ADAF ought to be very sharp (NKH, Manmoto & Kato 2000; Lu, Lin & Gu 2004). Such a sharp transition surface can also reflect acoustic waves, and thus the PPI may occur and result in the QPO in this system. We therefore argue that the QPO should be a common phenomenon in accretion flows with angular momentum. In particular, the QPO frequencies in a 3 : 2 ratio in black hole X-ray binaries (McClintock & Remillard 2006) may be explained by this instability for both $m = 2$ and $m = 3$ dominance, such as cases 2 and 7 (as shown in Fig. 3).

ACKNOWLEDGMENTS

We thank Thierry Foglizzo for helpful discussions. This work is supported by the National Science Foundation of China under Grant Nos. 10233030 and 10503003, and by the Natural Science Foundation of Fujian Province under Grant No. Z0514001.

REFERENCES

Blaes O. M., 1987, MNRAS, 227, 975
Blaes O. M., Hawley J. F., 1988, ApJ, 326, 277
Chakrabarti S. K., Das S., 2004, MNRAS, 349, 649
Foglizzo T., 2001, A&A, 368, 311
Foglizzo T., 2002, A&A, 392, 353
Foglizzo T., Tagger M., 2000, A&A, 363, 174
Fukue J., 1987, PASJ, 39, 309
Goldreich P., Narayan R., 1985, MNRAS, 213, 7
Goldreich P., Goodman J., Narayan R., 1986, MNRAS, 221, 339
Gu W. M., Foglizzo T., 2003, A&A, 409, 1 (Paper I)
Gu W. M., Lu J. F., 2004, Chin. Phys. Lett., 21, 2551
Kato S., 1987, PASJ, 39, 645
Lu J. F., Gu W. M., Yuan F., 1999, ApJ, 523, 340
Lu J. F., Lin Y. Q., Gu W. M., 2004, ApJ, 602, L37
McClintock J. E., Remillard R. A., 2006, in Lewin W. H. G., van der Klis M., eds, Compact Stellar X-ray Sources. Cambridge Univ. Press, Cambridge, in press (astro-ph/0306213)
Manmoto T., Kato S., 2000, ApJ, 538, 295
Molteni D., Tóth G., Kuznetsov O. A., 1999, ApJ, 516, 411 (MTK)
Nakayama K., 1992, MNRAS, 259, 259
Nakayama K., 1994, MNRAS, 270, 871
Narayan R., Goldreich P., Goodman J., 1987, MNRAS, 228, 1
Narayan R., Kato S., Honma F., 1997, ApJ, 476, 49 (NKH)
Narayan R., Mahadevan R., Quataert E., 1998, in Abramowicz M. A., Björnsson G., Pringle J. E., eds, Theory of Black Hole Accretion Disks. Cambridge Univ. Press, Cambridge, p. 148
Nobuta K., Hanawa T., 1994, PASJ, 46, 257
Paczyński B., Wiita P. J., 1980, A&A, 88, 23
Papaloizou J. C. B., Pringle J. E., 1984, MNRAS, 208, 721
Shakura N. I., Sunyaev R. A., 1973, A&A, 24, 337
Yuan F., 1999, ApJ, 521, L55

This paper has been typeset from a TEX/LATEX file prepared by the author.